Int. J. Electrochem. Sci., 15 **(2020)** 1788 – 1795, doi: 10.20964/2020.02.17

International Journal of
ELECTROCHEMICAL
SCIENCE
www.electrochemsci.org

Effect of the Particle Size of Cladding Materials on the Morphology and Corrosion Resistance of Fe-based Laser Cladding Layers

Chuanwei Shi[*], *Peng Liu, Dongfang Yan, Yuanbin Zhang*

School of Materials Science and Engineering, Shandong Jianzhu University, Jinan, China
[*]E-mail: shichuanwei@sdjzu.edu.cn

Received: 7 September 2019 / *Accepted:* 22 November 2019 / *Published:* 31 December 2019

Fe-based laser cladding layers were reinforced by TiC with different morphologies prepared in situ by using FeTi30 powder, graphite powder, and Fe-based self-fluxing alloy powder with different particle sizes. The effects of the particle size of the cladding alloy powder on the TiC morphologies, and the hardness and corrosion resistance of the reinforced Fe-based cladding layers were studied by X-ray diffraction, scanning electron microscopy, and an electrochemical workstation. The results showed that as the particle size of the cladding alloy powder decreased under the same laser cladding process, the cladding layer showed a better form, and there were no changes in the cladding layer phase. The TiC morphology changed from a large petal shape to a polygonal block. The hardness of the cladding layer decreased, but the corrosion resistance of the cladding layer increased.

Keywords: laser cladding; TiC; corrosion resistance; powder size

1. INTRODUCTION

Laser cladding, as a surface strengthening and repairing technology, can significantly improve the surface properties of a matrix. Laser cladding not only allows specific performance requirements to be met but also saves many precious alloying elements [1-3]. In situ reinforcement phases are obtained during the melting state of the laser cladding process, and obtaining ceramic particle reinforced metal-based cladding layers and improving the hardness and wear resistance of the material [4, 5]. At present, the reported in situ reinforcement phases used are mainly TiN [4], TiC [6, 7], VC [8, 9], WC [10], Al_2O_3 [11], and TiB_2[12]. Among these, TiC has characteristics of high hardness, high melting point, high corrosion resistance, and stable thermomechanical properties, making it an ideal ceramic reinforcement phase [13, 14]. Previous studies regarding TiC in the surface engineering field have mainly concentrated on argon arc cladding [15-17], thermal spraying [18, 19] and laser cladding methods.

X. Xu et al. [20] showed that there was a significant improvement in the microhardness and tensile strength of TiC-reinforced Inconel 625 coatings compared with that of pure Inconel 625 coatings. The TiC-reinforced Inconel 625 coatings also exhibited good corrosion resistance, demonstrating a further surface improvement of the ASIS 316L stainless-steel substrate. Ali Emamian et al. [21] reported that the laser parameters played a crucial role in establishing TiC morphology through temperature and chemical composition. It has also been reported that the dendrite morphology of the composite layer was changed to a cellular grain structure by increasing the laser pulse duration and irradiated energy, owing to more dissolution of carbon into the liquid Ti by the increase in the heat input and the positive influence of the Marangoni flow in the melted zone [22]. As the weight percentage of Ti+C increased, the peak temperature of the molten pool increased, which gradually increased the TiC particle size with the microstructure exhibiting a dendritic structure; in contrast, TiC/Inconel 718 composite layers with a fine dispersal of TiC particles exhibited high hardness and good wear characteristics compared to those with a dendritic structure [23]. There are limited studies regarding the relationship between the particle size of the cladding alloy powders and the properties of the TiC/Fe laser cladding layers. Therefore, the objective of the present study was to examine the effects of the particle size of cladding powders on the in situ TiC morphologies and properties of Fe-based laser cladding layers.

2. MATERIALS AND METHODS

Low carbon steel was used as the substrate material. Cladding alloy powders were composed of 39.47 wt.% Fe based self-fluxing alloy powder, 53.33 wt.% FeTi30, and 7.20 wt.% graphite (99.50% purity). The chemical compositions of the Fe based alloy powder and the FeTi30 powder are respectively listed in Table 1 and 2. The particle sizes of the cladding alloy powders are listed in Table 3. Mixed powders were placed on the low carbon steel surface using a sodium silicate binder and the thickness of the precursor was approximately 1.0 mm. Laser cladding was performed using a Laserline LDF-4000 semiconductor laser. The optimized laser power, laser beam diameter, scanning speed, and overlapping ratio were 2050 W, 4.0 mm, 5.0 mm/s, and 25%, respectively.

Table1. Chemical composition of the Fe based self-fluxing alloy powder

Cr	Ni	Si	B	C	Fe
12.0-14.0 wt.%	28.0-30.0wt.%	2.0-3.5 wt.%	1.0-2.0 wt.%	0.7-0.8 wt.%	Bal.

Table 2. Chemical composition of the FeTi30 alloy powder

Ti	Al	Si	C	P	S	Fe
26.15 wt.%	7.10 wt.%	4.50 wt.%	0.09 wt.%	0.05 wt.%	0.03 wt.%	62.08 wt.%

Table 3. Particle size of the cladding alloy powders

Samples	Fe based alloy powder	FeTi30 powder	Graphite powder
S1	45-106 μm	180-270 μm	180-270 μm
S2	45-106 μm	75-150 μm	75-150 μm
S3	45-106 μm	23-38 μm	23-38 μm

The layer phases were analyzed by X-ray diffraction with a Shimadzu-6100 diffractometer (Cu Kα) set to a working voltage and current of 40 kV and 30 mA, respectively. The step speed was 6 °/min. The microstructure and morphology of the cladding layer were observed using a ZEISS SUPRA55 scanning electron microscope with a tube voltage of 15 kV. Microhardness analysis was performed with a load of 1.96 N. Polarization curves of cladding layers were measured in 3.5 wt.% NaCl solution at 298 K, and were conducted with a scan rate of 0.5 mV/s using a Gamry electrochemical workstation (Interface 1000). A saturated calomel electrode was used as the reference electrode, and a platinum electrode was used as the counter electrode. The corrosion morphologies of the cladding layers after running the polarization curves tests were observed with the scanning electron microscope.

3. RESULTS AND DISCUSSION

Figure 1 shows the macromorphologies of the S1 and S3 cladding layers. The cladding layers showed good formation with the above two particle sizes of cladding alloy powders. The uneven surface of the S1 cladding layer may be due to an improper overlapping ratio, while the surface of the S3 cladding layer was relatively flat, which indicated that a fine particle size of the cladding alloy powder was beneficial for better formation of the cladding layer under the same heat input conditions. Daichi et al. [24] also confirmed that the smaller the alloy powder size, the better the layer formation. As the particle size decreased, on the one hand, the decrease of the particle radius led to an earlier melting time [25]; on the other hand, the specific surface area of the powder increased [26, 27], which increased the laser absorption efficiency during laser cladding. As a result, the utilization rate of the laser heat was greatly improved. Therefore, the surface forming quality of the S3 cladding layer was more ideal.

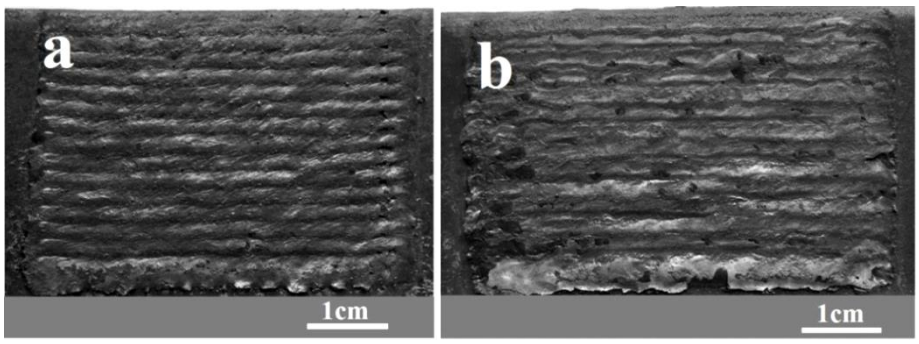

Figure 1. Macroscopic morphologies of the (a) S1and (b) S3 cladding layers

Figure 2 shows the X-ray diffraction spectra of the cladding layers. Phase analysis showed that the phases in the three cladding layers were alpha-Fe and TiC. Therefore, the TiC was formed by an in situ reaction of the Ti and C atoms during the laser cladding process. Thus, as the particle size of the cladding alloy powder varied within the range used in the present study, there were no changes in the phase of the cladding layers. In addition, the relative intensity of the TiC diffraction peak decreased from S1 to S3, which may be attributed to the oxidation of the graphite and titanium elements.

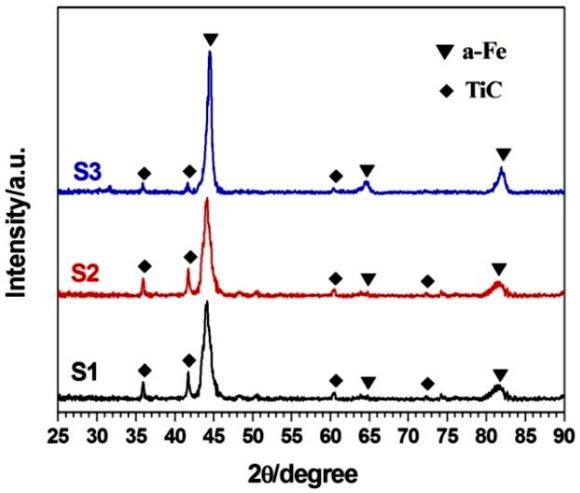

Figure 2. XRD spectra of S1-S3 cladding layers

Figure 3 shows the secondary electron morphologies of the cladding layers and the average particle size of TiC. Combined with the X-ray diffraction results, the black second phase was the TiC obtained by the in situ synthesis. Further analysis showed that the distribution of TiC in the S1 cladding layer was not uniform, some were petal-shaped and some were aggregated. The average size of the aggregates was approximately 7.56 μm. The distribution uniformity of the TiC in the S2 cladding layer was improved, and the distribution of the TiC was also aggregated. However, the size of the aggregates decreased significantly to approximately 2.13 μm. The distribution of the TiC in the S3 cladding layer was more uniform, and the morphologies changed to a polygonal block, with an average particle size of approximately 1.38 μm; furthermore, a large number of submicron scale TiC appeared in this cladding layer. Ali Emamian et al. [21] noted that the morphologies of in situ TiC could be varied from dendritic to spherical by adjusting the laser parameters, showing the TiC morphologies were actually controlled by the temperature and chemical composition. S. Corujeira Gallo et al. [28]also found that the morphology of TiC precipitates was affected by the chemical composition of the iron matrix for Fe-TiC. The size and volume fraction of TiC increased with increasing heat input and decreasing cooling rate in plasma transferred arc welding.

Because the particle size of the S1 alloy powders was relatively large, there was a large carbon concentration difference in the cladding layer, and the carbides grew and nucleated around the position of the graphite. With a decrease in the particle size of the cladding powder, the distribution of the carbide

forming elements in the molten pool was more uniform; thus, the nucleation number increased, the particle size of the carbide decreased, and the distribution tended to be uniform.

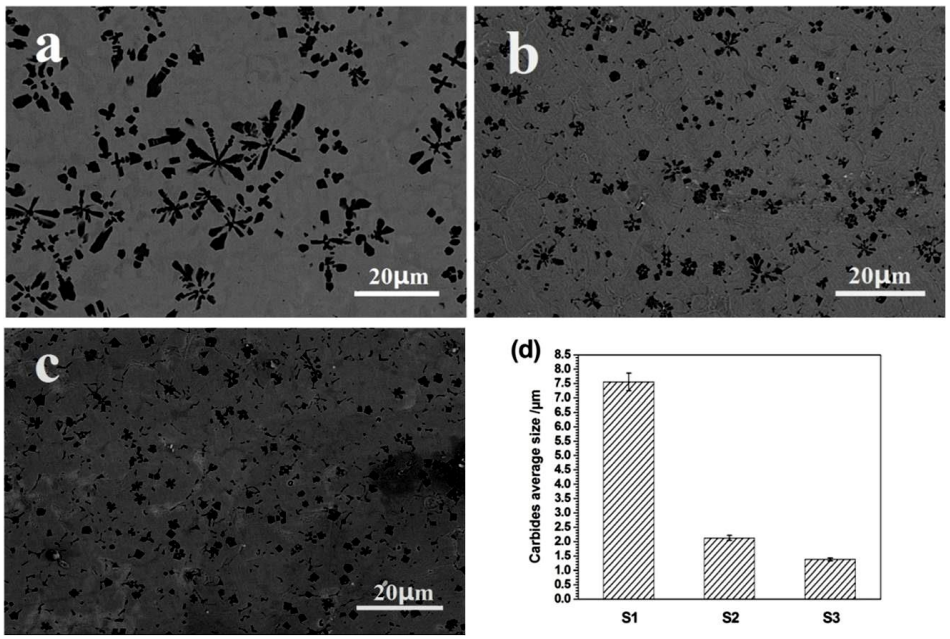

Figure 3. Secondary electron images of (a) S1 (b) S2 (c) S3 layers and (d) the average size of TiC

Figure 4 shows the microhardness distribution curve in relation to the depth of the cladding layers. The average hardness of the S1, S2, and S3 cladding layers were 867 HV0.2, 840 HV0.2, and 675 HV0.2, respectively. The hardness of the cladding layers decreased with decreasing the alloy powder size. The main reason for this decrease was that the decrease in the particle size of the alloy powder caused the burning loss of graphite to increase during cladding. Therefore, there was a decrease in the carbon content of the cladding layer. In addition, the microhardness of S1 fluctuated, which could be due to the aggregation of the TiC in the S1 cladding layer.

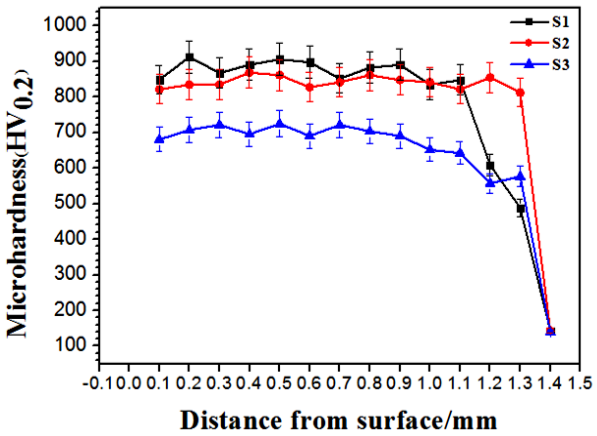

Figure 4. Microhardness distribution curves on the cross section of S1-S3 cladding layers

Figure 5 shows the polarization curve of the cladding layers in 3.5 wt.% NaCl solution. A traditional Tafel method was used to fit the curves. The fitting results are shown in Table 4. I_0 is the corrosion current density, and E_0 is the corrosion potential. From the fitting results, the corrosion potential of the cladding layer positively shifted from the S1 to S3 cladding layers, indicating that the corrosion tendency of the cladding layer decreased gradually. From the changes in the corrosion rate, the corrosion resistance of the cladding layers increased gradually. The above changes can be attributed to the changes in the morphologies and distributions of TiC.

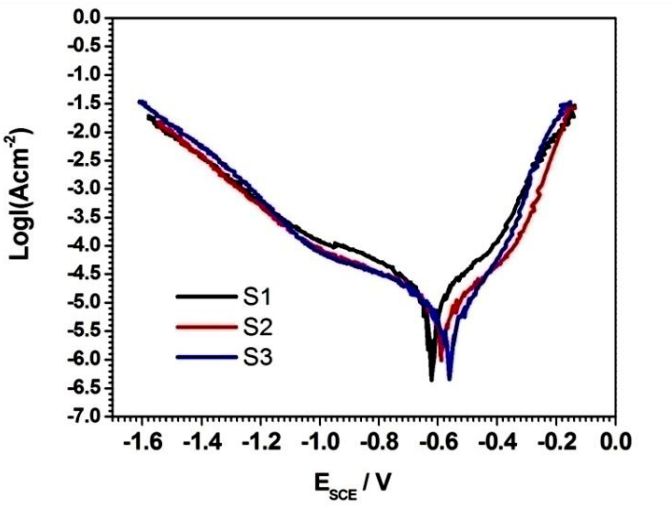

Figure 5. Polarization curves of S1-S3 cladding layers in 3.5wt.% NaCl solution

Table 4. Fitting results of the polarization curves

Samples	I_0/(μA/cm^2)	E_0/V	Corrosion rate/(mm·a^{-1})
S1	55.80	-0.6162	0.6503
S2	39.86	-0.5840	0.4645
S3	13.37	-0.5605	0.1558

Because the corrosion potential of TiC was higher than that of the cladding layer matrix, galvanic corrosion occurred readily in a corrosive medium, in which the TiC served as the cathode. The larger size of the carbide in the S1 cladding layer indicated that the cathode area was larger, which caused the galvanic corrosion to be stronger. As the size of the carbide decreased, the single galvanic corrosion weakened, especially in the S3 cladding layer where there were many more submicron TiC particles; thus, small cathode and large anode galvanic cells were produced, which significantly reduced the galvanic corrosion. Consequently, the corrosion tendency of the cladding layer was reduced, and the

corrosion resistance improved. K. Chong et al. [3] also indicated that the enlarged particle size of (Ti-V)C increased the galvanic corrosion that was generated between the carbides and the matrix layer.

Figure 6 shows the corrosion morphologies of the S1 and S3 cladding layers. Dramatic matrix corrosion of the S1 cladding layer was found, and the carbide morphologies were intact. The corrosion behavior mainly occurred at the interface between the carbide TiC and the matrix of the cladding layer, especially around the large carbide particles. The surface of the S2 cladding layer was relatively flat. Some of them occurred around the carbide aggregation position, and the other part occurred at the grain boundary. The results showed that the main corrosion type in the cladding layer was galvanic corrosion. When the carbide size was large, corrosion occurred between the carbide and the matrix of the cladding layer. When the carbide size was small, corrosion occurred between the matrix of the cladding layer and its grain boundaries.

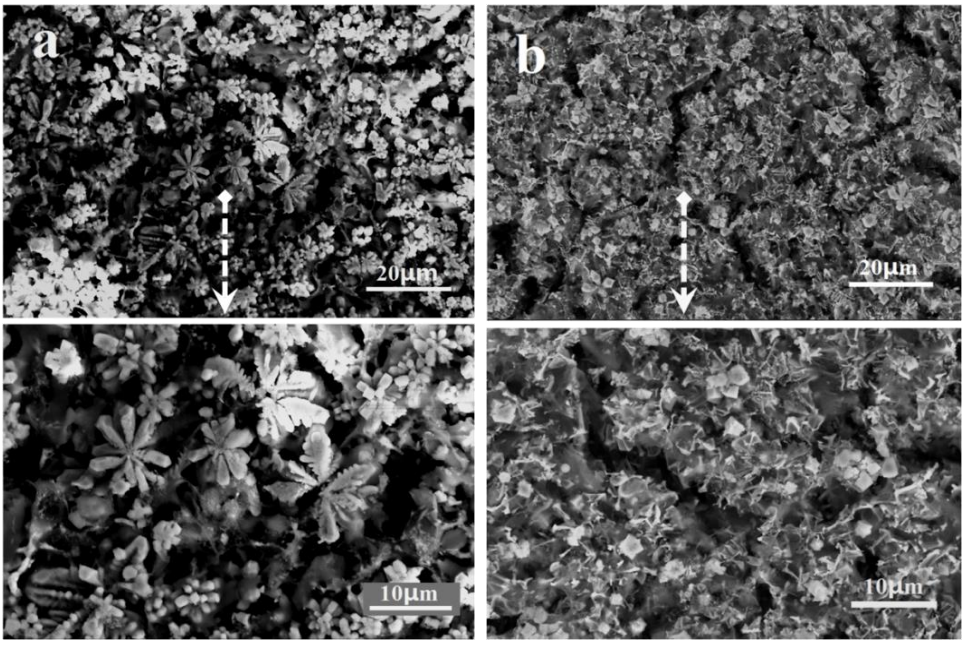

Figure 6. Corrosion morphologies of (a) S1 (b) S3 cladding layers after running potentiodynamic polarization curves tests

4. CONCLUSIONS

TiC-reinforced Fe-based laser cladding layers with different morphologies were prepared by an in situ reaction of Fe-based self-fluxing alloy powder, ferro-titanium powder, and graphite powder with different particle sizes. As the particle size of the cladding alloy powder decreased under the same laser cladding process, the cladding layer showed a better form, and there were no changes in the cladding layer phase. The morphology of TiC changed from a large petal shape to a polygonal block. The hardness of the cladding layer decreased, but the corrosion resistance of the cladding layer increased.

ACKNOWLEDGEMENT
The authors greatly appreciate the support of the Natural Science Foundation of Shandong Province (No.ZR2016EEB31).

References

1. L. Dubourg, J. Archambeault, *Sur. Coat. Technol.*, 202 (2008) 5863-5869.
2. Z. Zhang, T. Yu, R. Kovacevic, *Appl. Surf. Sci.*, 410 (2017) 225-240.
3. K. Chong, H. Zhang, G. Xiao, H. Xu, W. Zhao, *Int. J. Electrochem. Sci.,* 13 (2018) 6858-6869.
4. H. Liu, X. Zhang, Y. Jiang, R. Zhou, *J. Alloys. Compd.*, 670 (2016) 268-274.
5. X.H. Wang, L. Cheng, M. Zhang, S.Y. Qu, B.S. Du, Z.D. Zou, *Sur. Eng.*, 25 (2009) 211-217.
6. H. Zhang, K. Chong, W. Zhao, Z. Sun, *Sur. Coat. Technol.*, 344 (2018) 163-169.
7. H. Zhang, K. Chong, W. Zhao, Z. Sun, *Mater. Lett.*, 220 (2018) 44-46.
8. H. Zhang, K. Chong, G. Xiao, Z. Sun, W. Zhao, *Sur. Coat. Technol.*, 352 (2018) 222-230.
9. J. Zeisig, N. Schädlich, L. Giebeler, J. Sander, J. Eckert, U. Kühn, J. Hufenbach, *Wear*, 382-383 (2017) 107-112.
10. D. Shu, Z. Li, C. Yao, D. Li, Z. Dai, *Sur. Eng.*, 34 (2018) 276-282.
11. M. Sharifitabar, J.V. Khaki, M.H. Sabzevar, *Sur. Coat. Technol.*, 285 (2016) 47-56.
12. M. Masanta, S.M. Shariff, A. Roy Choudhury, *Mater. Design,* 90 (2016) 307-317.
13. J. Li, C. Chen, T. Squartini, Q. He, *Appl. Surf. Sci.*, 257 (2010) 1550-1555.
14. M.J. Hamedi, M.J. Torkamany, J. Sabbaghzadeh, *Opt. Lasers. Eng.*, 49 (2011) 557-563.
15. C.K. Sahoo, L. Soni, M. Masanta, *Sur. Coat. Technol.*, 307 (2016) 17-27.
16. C.K. Sahoo, M. Masanta, *J. Mater. Process. Technol.*, 240 (2017) 126-137.
17. S. Saroj, C.K. Sahoo, M. Masanta, *J. Mater. Process. Technol.*, 249 (2017) 490-501.
18. D. Hong, Y. Niu, H. Li, X. Zhong, W. Tu, X. Zheng, J. Sun, *Sur. Coat. Technol.*, 374 (2019) 181-188.
19. H. Ghazanfari, C. Blais, H. Alamdari, M. Gariépy, S. Savoie, R. Schulz, *Sur. Coat. Technol.*, 360 (2019) 29-38.
20. X. Xu, G. Mi, L. Xiong, P. Jiang, X. Shao, C. Wang, *J. Alloys. Compd.*, 740 (2018) 16-27.
21. A. Emamian, S.F. Corbin, A. Khajepour, *Sur. Coat. Technol.*, 206 (2011) 124-131.
22. M.J. Hamedi, M.J. Torkamany, J. Sabbaghzadeh, *Opt. Lasers. Eng.*, 49 (2011) 557-563.
23. G. Muvvala, D. Patra Karmakar, A.K. Nath, *J. Alloys. Compd.*, 740 (2018) 545-558.
24. D. Tanigawa, N. Abe, M. Tsukamoto, Y. Hayashi, H. Yamazaki, Y. Tatsumi, M. Yoneyama, *Opt. Lasers. Eng.*, 101 (2018) 23-27.
25. Y. Shi, Y. Zhang, C. Konrad, *Nanosc. Microsc. Therm. Eng.,* 11 (2007) 301-318.
26. J.C. Heigel, M.F. Gouge, P. Michaleris, T.A. Palmer, *J. Mater. Process. Technol.*, 231 (2016) 357-365.
27. C. Y. Liu, J. Lin, *Opt. Laser. Technol.,* 35 (2003) 81-86.
28. S. Corujeira Gallo, N. Alam, R. O'Donnell, *Sur. Coat. Technol.*, 225 (2013) 79-84.